POLITECNICO
MILANO 1863

SCUOLA DI INGEGNERIA INDUSTRIALE
E DELL'INFORMAZIONE

# Dissecting Cabozantinib mechanisms of action and therapeutic efficacy in preclinical models of prostate and renal cancer lesions in bone

TESI MAGISTRALE IN BIOMEDICAL ENGINEERING

**Busà, Silvia, 10803364**

**Advisor:**
Pietro Cerveri

**Co-advisors:**
Eleonora Dondossola

**Academic year:**
2023-2024

**Abstract:** **Prostate and renal cancers have become a major issue among cancer-related mortality in Western countries and their prevalence is expected to rise worldwide. Both tumors tend to metastasize especially in bone, and once cancer has spread to the bones it can be rarely cure. Bone metastasizes lead to a sever and painful condition for the patient and among treatments option, cabozantinib represents a cost-effective option that it has been approved for the metastatic renal cell carcinoma treatment and is being considered for prostate cancer. This agent is a VEGF receptors tyrosine kinase inhibitor that inhibits tumor neo angiogenesis. This study aims to investigate the effects of cabozantinib on bone lesions due to prostate cancer and whether they are comparable to the effects on bone lesions due to renal cancer.** A **newly developed preclinical model was applied to gather data from the prostatic model, nude mice were engrafted with human-derived tumor cells followed by oral administration of cabozantinib, while data for the renal model were already available. Since cabozantinib is an anti-angiogenic agent, the analysis was focused on changes of blood vessel's structure and its impact on tumor cell proliferation. The evidence collected from this study demonstrates that cabozantinib has similar effects in both tumors, affecting the blood vessel's structure independently from the tumor cells involved. Indeed, it affected by 3% and by 9% the blood vessels density in the prostate and renal model respectively, while decreasing the lengths and widths by 40% and 88% in the first and by 75% and 66% in the second model. Importantly, conducting this analysis highlighted the current lack of automatic tool able to recognize mitotic and apoptotic events within biological images, resulting in a manual time-consuming process performed by expert personnel. Consequently, I started to work on an artificial intelligence-based system able to automatically discriminate mitosis and apoptosis within ground truth images.**

**Keywords: prostate cancer, renal cancer, cabozantinib, blood vessels, mitotic tumor cells**

# 1. Introduction

Prostate cancer is the second most diagnosed cancer in men and sixth leading cause of related cancer death among men globally, but an even more common cause of cancer-related mortality in Western countries [1]. Renal cell carcinoma (RCC) stands as the most prevalent form of kidney cancer. This type of cancer, accounts for about 2% of cancer cases and cancer-related deaths globally. Its prevalence is expected to rise worldwide [2] [3]. Both prostate and renal tumors are known for their tendency to metastasize, and bone represents a major site of colonization [4]. The relative incidence of bone metastases in patient with advanced prostate cancer is 65-75% while in patient with advanced RCC is 25-40%. Once cancer has spread to the bones it can be rarely cured, and patient survival is only prolonged for a limited time; the median-survival from diagnosis of bone metastasis is 12 months in RCC and 12-53 months in prostate [4] [5]. Bone metastases are a major cause for morbidity, characterized by severe pain, impaired mobility, pathologic fractures, spinal cord compression, bone marrow aplasia, cranial nerve palsies, nerve root lesion, and hypercalcemia [4]. Bone metastasis can be detected with X-ray, bone scintigraphy (bone scan), computer tomography (CT), or with high sensitivity methods including whole body magnetic resonance imaging (MRI) and positron emission tomography-computed tomography (PET-CT [6]). X-ray, bone scan, and CT detect the presence of skeletal pathology but gives little information about its nature. Structural information from metastatic lesion is best obtained by MRI and PET-CT.

Treatment decisions depend on several parameters, for example, if and where bone disease is localized or widespread, if there is evidence of extra skeletal metastases, the kind of cancer and his features, prior treatment history and disease response, the symptoms, and the general state of health. However, treatments can often shrink or slow the growth of bone metastases and can help with the symptoms they are causing but they are not curative [4]. Among the palliative treatments, external beam radiotherapy in combination with analgesic is the basic option and is mostly indicated for pain relief for its minor side effects and its ability to act directly against the cause of bone pain. When classical radiotherapy is not practical, radiopharmaceuticals such as radium-223 may be applied instead, especially in bone metastases from prostate cancer [6]. Radium-223 is a calcium mimic, that incorporates into bone and forms complexes with the mineral hydroxyapatite at the areas of bone metastases. Its high energy $\alpha$-particles induce breaks to DNA, cell cycle arrest, and eventually death of cells, and suppression of tumor-induced pathologic bone formation [1]. However, hematological toxicity or disease progression is commonly observed during this therapy. Other treatment option specific for advanced and metastatic prostate cancer are represented by: hormonal therapy, or androgen deprivation therapy (ADT), where the therapeutic mechanism is based on the blockage of testosterone production and other male hormones, preventing them from fueling prostate cancer cells; the administration of Abiraterone, approved from FDA in 2011 as a second-generation therapy targeted at adrenal and tumor androgen production; the immunotherapy, or biological therapy based on stimulating or suppressing the immune system; combination therapy, usually ADT with Abiraterone or immunotherapy. All of them have side effects including edema, fatigue, hypertension, hypokalemia and despite the various treatment options, metastatic prostate cancer remains to be an incurable disease. [7] Regarding metastatic renal cell carcinoma (mRCC), available interventions include various anti-angiogenic tyrosine kinase inhibitors that target vascular growth factor receptor (VEGFR) receptor, and immunotherapies, but although these drugs may improve overall survival, complete remission is rare, and advanced renal cell carcinoma remains a deadly disease. Among VEGF receptor tyrosine kinase inhibitors, cabozantinib represents a cost-effective option in first line treatment of mRCC, approved from FDA. Specifically, cabozantinib is a multi-

target inhibitor of tyrosine kinases which, in addition to inhibiting VEGF receptor, also acts at the level of other proteins, such as MET and AXL implicated in the mechanisms of tumor progression and resistance [8]. Cabozantinib in preclinical models has demonstrated notable effects on tumor growth by limiting blood vessel formation. [5] [9]. Because of these effects on the tumor microenvironment, cabozantinib is being evaluated in clinical trials in bone metastases from other solid tumors (such as castration-resistant prostate cancer), and analysis is evaluated i.e. based on ultrasound, MRI data, tissue microarrays signals, cell proliferation, gene expression [10] [11] [12].

The objectives of this study are to investigate the effects of cabozantinib on blood vessels within bone metastases from prostate tumor and to evaluate whether effects of cabozantinib in RCC and prostate cancer are comparable. Indeed, despite being approved for RCC treatment, cabozantinib effects on bone lesions are obscure, mostly due to the absence of relevant models of bone metastasis and, moreover, a comparison between blood vessels changing in prostate vs renal bone metastasis after cabozantinib treatment was never performed. In this study, a newly developed preclinical model specific for bone metastasis was applied, using human-derived prostatic tumor cells (PC3) engrafted into nude mice tibiae, followed by oral administration of cabozantinib. The analysis was performed using ex vivo images from multiphoton microscopy (MPM) acquisitions, that allowed blood vessels parameters assessment within the tumor area, including the percentage of area occupied by blood vessels, their shape and size, the distance between proximal blood vessels, and the proximity of a mitotic cell to the nearest blood vessel. The findings from this study are crucial in understanding the drug's potential effects on the vascular structures within bone metastases and may provide valuable insights into its efficacy across different cancer types. Moreover, this study underscored the challenge of manually identifying mitotic and apoptotic cells in biological images and prompted the development of a new artificial intelligence-based system for the automatic recognition and quantification of mitotic and apoptotic nuclei, in collaboration with the Department of Electronics, Information and Bioengineering.

# 2. Material and Methods

## 2.1 Study Design

Mice bearing prostate cancer bone lesions were orally administered cabozantinib, bone were then isolated and analyzed by immunofluorescence analysis. The focus was on studying the impact of this agent on the vascular structure of bone metastasis; different parameters were quantified, including the percentage of blood vessel area within the tumor region, vessels dimension, inter-vessel distance, and the proximity of mitotic cells to vessels. To validate our findings, bone lesions from renal tumor previously collected by Dr. Dondossola's laboratory team were also analyzed.

While performing this study, especially the manual identification of mitotic cells in tumor lesions, the need for an automatic analysis tool became evident. Therefore, a neural network-based system to detect mitotic and apoptotic nuclei was developed, which required manual segmentation of original images to train the neural network. Therefore, several in vitro experiments were conducted to generate these images.

## 2.2 Cell Lines and Culture

### 2.2.1 PC3 Cell Line

The PC3 cell line was isolated from a patient with metastatic prostate cancer. This cell line is well suitable for the pre-clinical studies because the cells are androgen-independent (the androgen hormone is no needed for the growth), they present rapid and easy to maintain growth in vitro [13]. PC3 used in the lab of MD Anderson Cancer Center are dual color (DC), i.e. genetically modified to emit in the red wavelength the cytoplasm and in the green wavelength the nucleus. PC3 were grown in a standard cell culture flask in 18 ml of DMEM, in an incubator at 37 C, 5% $CO^2$.

### 2.2.2 RENCA Cell Line

The RENCA cell line was developed from a spontaneous renal cell carcinoma of a BALB/c mouse. It is widely used in the laboratory to study tumor oncogenesis because it forms tumors in vivo when transplanted into immunocompetent mice of the same strain (BALB/c). They were grown in a standard cell culture flask in 18 ml of DMEM, in an incubator at 37 C, 5% $CO^2$.

## 2.3 EVOS Imaging System

The EVOS imaging system includes a multichannel fluorescence or brightfield microscope and a supporting software. EVOS allows time-lapse movie acquisition, multi-well plate scanning, image stitching and tiling and cell counting, providing high quality images in no time, over time, every time [14]. The EVOS system in this work was widely used to characterize PC3 cell line. It was extensively used to capture images and videos during various experiments. These experiments involved plating cells at different dilutions and treating them with three distinct drugs at varying concentrations.

### 2.3.1 Plating of PC3 in Serial Dilution in a 24 Well Plate

From a standard cell culture flask, the medium was removed with a vacuum or a pipet controller. Cells were washed with 10 ml of PBS (at least 2 times); 3 ml of trypsin in the flask was added and the flask was left inside the incubator for 3 min. After 3 min, a check under microscope was done to see if the cells inside the flask were dethatched and, if necessary, the flask was tapped to ensure the detachment of all of them. Then, 7 ml of DMEM to block the trypsin was added. The total volume was put inside a 50 ml tube Falcon and the mixture was shaken well. Lately, 10 µl from the mixture and 10 µl of trypan blue were taken and both were put inside a 500 µl tube Eppendorf and mixed well. After that, 10 µl from the Eppendorf was taken and the solution was added to a disposable slide for cell counting. A cell counter was used to determine how many cells per unit of volume there was in the Falcon's solution and so how much volume of that mixture was needed (number of cells counted: unit of volume = total number of cells needed: start volume of mixture). For this experiment $20x10^3$ cells was the total number needed.

A serial dilution 1:2 in 800 µl of DMEM was performed in six of the 24 well plate: first well with $20x10^3$ cells, second well with $10x10^3$ cells, third well with $5x10^3$ cells, fourth well with $2{,}5x10^3$ cells, fifth well with $1{,}25x10^3$ cells, sixth well with 625 cells. One day after seeding the cells, acquisition with the EVOS system was performed. In particular: time lapse of 24h from a specific area of 3 different well, photos of the hall 6 well at 1 day, 2 days and 3 days after the seeding. In both cases the acquisition was performed with 3 channels, one feature each of them: nucleus, cytoplasm, and phase. From the time lapse it was possible to study the kinetics of mitosis and apoptosis, how cancer cells increase over time, the percentage of mitotic cells.

### 2.3.2 Cell Treatment with Serial Dilution of Doxorubicin (2mg/ml), Docetaxel (20mg/ml), Cisplatin (1mg/ml) in a 96 Well Plate

At the beginning, $5x10^3$ cells were seeded in 100 µl of DMEM in the first half of the plate (48 well), $10x10^3$ cells were seeded in 100 µl of DMEM into the second half, then the cells were led to attach to the well for 4-24 h. The initial drug dilution was prepared within individual 1 ml tubes for each drug. Subsequently, all of them were diluted at a 1:3 ratio from tube 1 (max concentration) to tube 7 (lowest concentration). The eighth tube was containing only medium (control). The vortex was used to mix the solution between each dilution.

*Doxorubicin*: Induces apoptosis in cancer cells by binding to DNA-associated enzymes, intercalating the base pairs of the DNA's double helix [2]. Initially, as first concentration of 2.1 µl in 750 µl of DMEM was used. This was increased to 44 µl in 750 µl of DMEM as apoptosis was not observed at lower dilutions.

*Cisplatinin*: induce apoptosis of cancer cells by crosslinking with the purine base on the DNA; interfering with DNA repair mechanism, causing DNA damage, and subsequently apoptosis in cancer cells [15]. The first initial concentration was 2.25 µl in 750 µl of DMEM, subsequently raised to 44 µl in 750 µl of DMEM to induce more apoptosis at lower dilutions.

*Docetaxel*: induce apoptosis of cancer cells by promoting and stabilizing microtubule assembly while simultaneously preventing microtubule depolymerization [16]. The starting concentration was 3µl in 750 µl of DMEM.

Once the eight dilutions for each drug was ready, the DMEM from the 96 wells of the plate was aspirated, being careful not to disturb the attached cells. The rows were filled with drugs as follows: the first two wells A1, A2 with the highest concentration of Doxorubicin, the next two A3, A4 with the highest concentration of Cisplatinin, and wells A5, A6 with the highest concentration of Docetaxel. Wells A1 and A2 with the highest concentration of Doxorubicin, A3 and A4 with the highest concentration of Cisplatin, and A5 and A6 with the highest concentration of Docetaxel. This sequence was repeated for the remaining rows, ensuring the highest concentrations were placed in the same row for both sections initially seeded with $5x10^3$ and $10x10^3$ cells. Starting from row B, the same sequence was followed with lower dilutions of each drug (e.g., B1, B2 Doxorubicin from the second tube, B3, B4 Cisplatin from the second tube, etc.) for each subsequent row, ending with the eighth (last) row as the control group (no drugs). The plate was incubated and the EVOS imaging system was employed to capture images of the wells on days 1, 2, and 3 post-drug application. These images clearly show apoptotic phenomena.

## 2.4 In Vivo Studies

Animal studies were approved by the Institutional Animal Care and Use Committee of The University of Texas MD Anderson Cancer Center (MDACC) and performed according to the institutional guidelines for animal care and handling. 8-week-old, female nude mice were obtained from The Jackson Laboratory (Bar Harbor, ME, USA). Mice were housed with a maximum of 5 animals per cage in a state-of-the-art, air-conditioned, specific-pathogen–free animal facility. All the procedures described were performed in agreement with the NIH Policy on Humane Care and Use of Laboratory Animals. Surgeries were performed with mice under general anesthesia (isoflurane), and analgesia was provided for each procedure (buprenorphine slow release, 0.5 mg/kg, immediately before the start of the surgery). Tumor-bearing animals were observed daily and examined by a veterinarian 5 days/week for signs of morbidity (e.g., matted fur, weight loss, limited

ambulation, and respiratory difficulty). In case of discomfort, the animals were euthanized by asphyxiation with carbon dioxide gas followed by cervical dislocation, consistent with the recommendations of the Panel on Euthanasia of the American Veterinary Medical Association.

### 2.4.1 Tibiae Injection

The protocol we used was developed to minimize the invasiveness of the procedure for subsequent immune studies. It further shortens the procedure and uses inhalable anesthesia. Both factors make the procedure easier for the mice.

Material: cells in flask; 27 G needle for drilling the hole; 20 G needle for cell injections; 1ml syringes; isoflurane and mask; Buprenorphine (0,1 mg/kg); ethanol; cold light sources with double swan nek optical fiber, Schott/Leica KL 1500; 1 heating pad; 1 adsorbent under pad, iodine solution.

Method. Day of injection: cells were detached and transferred to 50 ml Falcon; the solution was centrifugated and the supernatant above the pellet was trashed; the pellet was agitated and resuspended in 45 ml of PBS; the mixture was centrifugated and the supernatant above the pellet was trashed; the pellet was agitated and it was resuspended in 45 ml of PBS; the cells were counted; 3,5 mln/ml cell suspension were prepared (inject 20 μl=350.000 cells).

The surgical hood was prepared. Buprenorphine was injected (0,1 mg/kg) subcutaneously in the mouse immediately before procedure; the mouse was anesthetized using isoflurane, then it was moved to nose cone while anesthesia was maintained; both legs were cleaned with ethanol, repeating 2 times, and they were disinfected with iodine solution; the cell solution previously prepared was sucked up with 1 ml syringe provided with 20 G needle; gently the lateral malleolus, medial malleolus, and lower half of tibia were grasped with forefinger and thumb, then the leg was bended; the skin was wet with 10% EtOH to increase visibility of underlying patellar ligament, which should be visible as a distinct, thick, white line. While firmly grasping ankle/leg of mouse a 27 G needle of a second 1 ml syringe was inserted under patella, through the middle of patellar ligament, and into the anterior intercondylar area in top of tibia; when we were inserting needle into tibia, we guided carefully through growth plate using steady, firm pressure with slight drilling action; upon penetration of tibial growth plate, the needle encountered markedly less resistance; a gentle, lateral movement of needle was used to ensure needle is in tibia and through the growth plate (movement is limited if needle is in proper place within tibia); slowly the needle was removed and pre-charged syringe with cells for the injection was used; the plunger was pressed slowly and 10-50 μl of cell solution was injected; little to no resistance should be felt at this point; the needle slowly was extracted; following the same procedure, we proceeded to next leg; the mouse was removed from anesthesia and kept on heating pad until he recovered; the mice was monitored over the next 72 hours.

### 2.4.2 Cabozantinb Preparation

Material: 1ml syringe, 20 G needle, Cabozantinib doses, marker.

Cabozantinib powder dose: 40 mg/kg/day. Here, a single mouse was 30 g, so 1,2 mg of powder per each mouse per day was used.

The single dose of cabozantinib powder had to be dissolved in 100mg of liquid composed of 7% DMSO, 30% PEG, 5% TWEEN, 58% water, following these steps:

- in a 1ml tube the total powder and the DMSO were put. Vortex was used to mix them well.
- a sonicator for 10 minutes was employed to let them melt.

- PEG and TWEET were added in the melted solution and the mixture was placed again in a sonicator for 10 minutes.
- Water was added and it was mixed.

One dose per each mouse was used every day for at least 7 days. In this work, two mice were treated for 7 days, while the other 3 mice for 10 days.

### 2.4.3 Gavage

Material: 1ml syringe, 20 G needle, Cabozantinib doses, marker.

Method. The tail of each mouse was marked to avoid treating the same one multiple times. The syringe was filled with the drugs and, each mouse was taken firmly, and the needle was gently introduced from the mouth to release the dose directly in the stomach. The needle was removed, and the mouse released.

### 2.4.4 Tibiae Extraction

Material: scissor and tweezer sterilized, under pad, one 15 ml tubes each mouse, isoflurane box, paraformaldehyde (PFA).

Method. The surgical hood was prepared. The mice were euthanized, and the tibiae extracted. Later the tibiae were put in a tube with 6ml of 4% PFA to fix them.

## 2.5 Sample Processing.

Material. Tubes with bones in PFA, agarose 4%, PBS, plastic tray, blade, superglue.

Method. The samples were prepared: the bones were washed from PFA. 4% w/v melting agarose was prepared (4g for 100ml PBS) and heated for 40 sec in the microwave. We waited 1 min for the agarose to cool down. The bone was placed in the little plastic tray and the agarose poured. We waited 5-10 minutes for the agarose to polymerize.

Vibratome procedure: the agarose block was removed with the included bone from the tray and the edges (with the blade) were cut to reduce the block dimensions. The glue was used to stich the block to the Vibratome's holder. We waited 5 min for the glue to work. The bone was orientated perpendicular to the vibratome's blade with the distal part of it (the one next to the next to the ankle) closer to the blade. The place was filled with PBS.

Vibratome settings. Speed 9, frequency 4, section 300 μm were set to cut perpendicular to the longitudinal axis of the bone; speed 9/8, frequency 5/6, section 150/200 μm were set to cut layer parallel to the longitudinal axis of the bone. The sections were sliced and collected with a small brush or the tweezers (holding the slices from the agarose part, not touching the section of the bone). They were put in a tray with PBS. The agarose could be easily peeled off the bone. They were stored in the fridge (4°C). We changed the vibratome blade every 3 bones cut.

## 2.6 Immunofluorescence Staining

Material. Staining solution: PBS base, 10% DMSO, 0.5% Igepal, 5% Donkey serum (the serum should match the species the secondary antibodies are made in), primary antibody, and secondary antibody.

Method. We blocked the samples in staining solution overnight. The primary antibody was added in staining solution at 1:200 dilution and the samples were incubated overnight at 4°C. Then, the samples were washed 5 times in PBS, over the course of an entire day. The secondary antibody solution was prepared in 300 μL staining solution the secondary antibody was added at 1:400 dilution together with DAPI (4',6-diamidino-2-phenylindole), to visualize nuclei. The plate was wrapped in aluminum foil and from this point on, the plate was kept dark/wrapped in foil as much as possible. The plate was incubated overnight at 4°C and finally washed 5 times in PBS over the course of an entire day.

## 2.7 Multiphoton Microscopy

Two-photon excitation microscopy, also known as non-linear or multiphoton laser scanning microscopy (MPM), offers an alternative approach to confocal microscopy. It excels at three-dimensional imaging, particularly for living cells within intact tissues. [17] Effectiveness of fluorescence microscopy in thick specimens is often limited by out-of-focus flare. Confocal microscopes try to overcome this limitation by employing a confocal pinhole, resulting in thin and clear optical sections (less than 1 micrometer). This technique enables three-dimensional sectioning in thicker tissues. However, the excitation light generates fluorescence, leading to photobleaching and phototoxicity across the specimen, despite collecting signals within the focus plane. This can significantly impact live specimens and the quality of the images over the time. Additionally, confocal microscopy's depth penetration is restricted due to energy absorption and specimen scattering of excitation and emission photons. [17]

In contrast, two-photon excitation offers three-dimensional optical sectioning without causing photobleaching or phototoxicity above and below the focus plane. That happen because the physical principle relies on the absorption probability (absorption depends on the square of the excitation intensity), which increases when a pulsed laser is focused through the microscope optics. This process concentrates photons spatially and temporally, allowing two photons to interact simultaneously with a single fluorophore. This interaction occurs only at the laser's focal point, where the photon density is sufficient. Below and above at this point, the photon density is insufficient for this interaction to happen. [17] Consequentially, compared to confocal microscopy, the major advantage of two-photon excitation is its precise localization to the illumination focal point [17]. Moreover, it allows more excitation light to penetrate through the specimen to the focus plane, reducing fluorescence scattering effects. This results in increased specimen penetration, typically two or three times more than achievable with confocal microscopy, thereby minimizing phototoxicity by confining photodamage to the focal volume. [17]

Due to these combined effects, two-photon excitation is particularly effective for imaging thicker specimens. The instrumental requirements for two-photon excitation microscopy are like those of confocal microscopy, except for the laser excitation source, which differs significantly. It requires a laser emitting ultrashort pulses (mode-locked) to enable simultaneous absorption of two or more photons, usually operating in near-infrared frequencies. [17] Multiphoton microscopes are expensive primarily because of their lasers, making maintenance challenging and costly. In this study, we utilized the MPM available at the MD Anderson Cancer Center genitourinary laboratory, and we obtained images from ex vivo animal samples. The images were then analyzed using the Image J software.

## 2.8 Data Analysis

Data analysis was performed using Fiji software, an open-source image processing tool based on ImageJ2 [18]. This software enabled the visualization and the quantification of images/video obtained from both the EVOS system and MPM acquisition. This involved quantifying various parameters such as the percentage of the area occupied by blood vessels within the tumor area, their size, the proximity of a mitotic cell to the nearest blood vessel and the distance between adjacent vessels. ImageJ was also used for the segmentation of biological images used to train the artificial intelligence-based system for the automatic recognition of mitotic and apoptotic nuclei.

### 2.8.1 Assessment of Parameters

The parameters studied are shown in Figure 1, in which each photo was captured using MPM, where green is for nuclei and red is for blood vessels (BVs). The parameters were calculated with ImageJ's support.

(a) *Percentage of Blood Vessels Within Tumor Area* (Figure 1a): it determines the proportion of the tumor area occupied by blood vessels. It is noteworthy that this may not always correspond to the entire area inside the bone matrix.

(b) *Blood Vessel Dimensions* (Figure 1b): analysis of blood vessels measuring both maximum length (L) and maximum width (W).

(c) *Proximity of Mitotic Tumor Cells to Nearest Blood Vessel* (Figure 1c)*:* it assesses the spatial relationship between mitotic tumor cells (MTC) and the nearest blood vessel.

(d) *Spatial Distribution Between Blood Vessels* (Figure 1d)*:* it analyzes the distances between blood vessels inside the microenvironment.

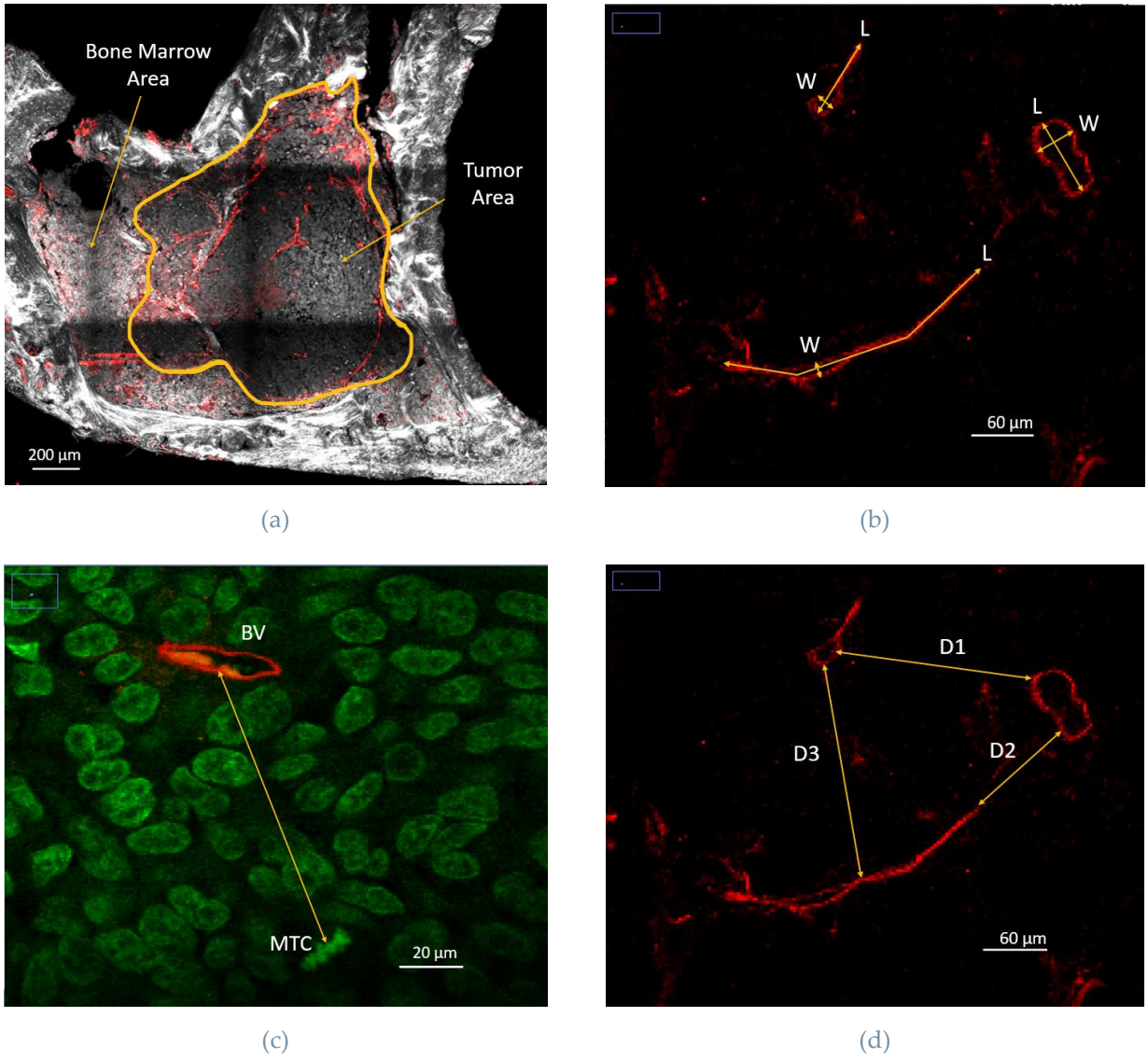


Figure 1: Evaluation parameters for metastatic bone microenvironment. (a) %BV inside tumor area: here a tibiae cross section with PC3 cells as tumor cells. PC3 are usually bigger than normal bone marrow cells. (b) BVs size; (c) MTC-BV distance; (d) BV-BV distances.

# 3. Results

## 3.1 In Vivo Studies

In order to study the impact of cabozantinb on blood vessels within bone metastases from prostate and renal tumors, in vivo studies were performed. Samples of bone metastatic renal cells were previously generated in the lab. Instead, to obtain data regarding prostate cancer bone metastases, new experiments were performed. Since human prostate cancer cells (PC3) were used, nude mice were applied. This specific mouse strain exhibits a congenital immunodeficiency resulting in the absence of a functional thymus and therefore it lacks mature T cells and possess a reduced count of circulating lymphocytes compared to wild-type or heterozygous controls [19]. This unique

immunological trait facilitates the engraftment of human cancer cells [19]. PC3 cells were directly injected into both tibiae; after 3 days, treated mice received cabozantinib by oral gavage (as described in the methods) and, after 7 or 10 days, control and treated mice were euthanized. Tumor-bearing bone were processed as reported in the next paragraphs.

### 3.1.1 Preparation of the Samples: Vibratome Sectioning, Immunofluorescence Staining, and Slicing Optimization

Tumor-bearing tibiae were extracted, fixed in 4% PFA for 24 hours, decalcified in 0.5 M EDTA for 5 days, and sectioned using a vibratome, a type of microtomes used for obtaining three-dimensional (3D) histological sections [20]. Specifically, for this analysis, bone samples embedded in agarose 4% were cut with a thickness of 100 μm. Then, slices were first stained (immunofluorescence) and subsequently captured at the multiphoton microscope (MPM).

Immunofluorescence (IF) analysis was used to visualize specific components of the bone samples, including cell nuclei and tumor blood vessels. Among the IF techniques, the indirect, or secondary, type was employed for staining blood vessels, because of its high sensitivity, signal amplification, and its ability to detect several targets in the same sample [21]. In the secondary type of IF, the staining procedure involves the use of two sequential antibodies, defined primary and secondary. The primary antibody derives from a different species than that of the sample, to prevent aspecific cross-reaction of the secondary antibody with endogenous immunoglobulins in the tissue sample. Before any antibody application, however, blocking must be performed on tissue samples to prevent antibodies from binding to non-target epitopes present [21]. At first, were employed rabbit anti-laminin (a marker of the basal lamina) primary antibody and anti-rabbit AlexaFluor 488 (green) made in donkey as secondary antibodies; however, the resulting fluorescence signal was not strong enough to clearly distinguish between blood vessels and noise. Then, we used different secondary anti-rabbit antibodies conjugated with AlexaFluor 546 (red) AlexaFluor 680 (far red), and evaluated the signal emitted in a different wavelength, but results were not significantly better. Finally, rat anti-endomucin (a specific marker of bone sinusoidal vessels) primary antibody combined with anti-rat AlexaFluor 680 made in donkey allowed to detect a specific signal. DAPI was applied to detect nuclei of PC3 tumor cells and bone marrow cells, which were easily distinguishable based on their size. PC3 cells, indeed, are ~8 times bigger than mouse bone marrow cells. An example of sample showing nuclei (green) and blood vessels (red) acquired at the MPM is reported in Figure 2 (A more detailed explanation about sample acquisition through MPM is detailed in paragraph 3.1.2). Nuclei of PC3 cells, which express GFP protein linked to the histone H2B, were also detected in the majority of experiments.

.

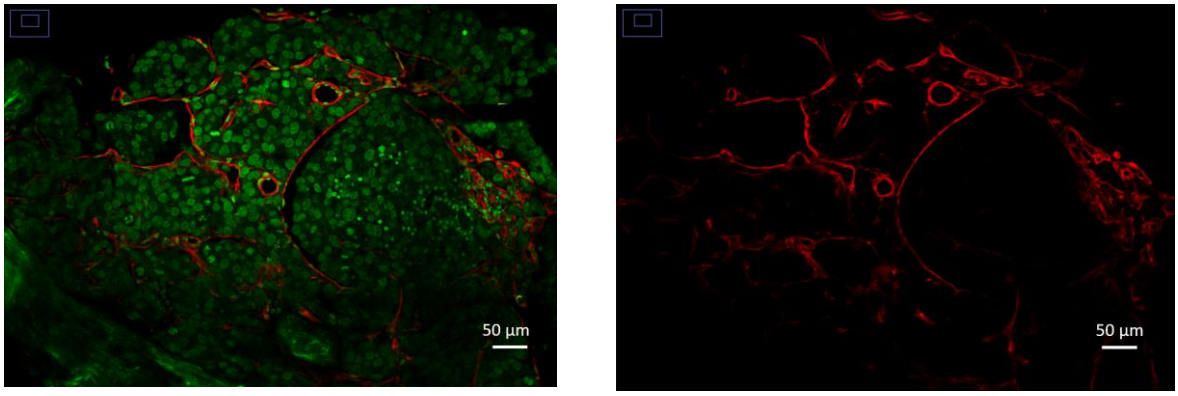


(a) (b)

Figure 2: Cross-section of a tibia injected with PC3 cells. (a) Blood vessels and nuclei. (b) Blood vessels stained with rat anti-endomucin as a primary antibody and anti-rat AlexaFluor 680 donkey as a secondary antibody. Nuclei were stained with DAPI.

In this study, decalcified bone samples were initially sliced parallel to the bone's longitudinal axis to obtain a bigger field of view (see Figure 3). When samples were cut parallel to this axis, however, visualizing the tumor blood vessels was challenging, due to the high number of intertwined blood vessels which tended to surround the tumor mass. Therefore, transversal slicing was then performed, to better visualize the blood vessels within the tumor mass.

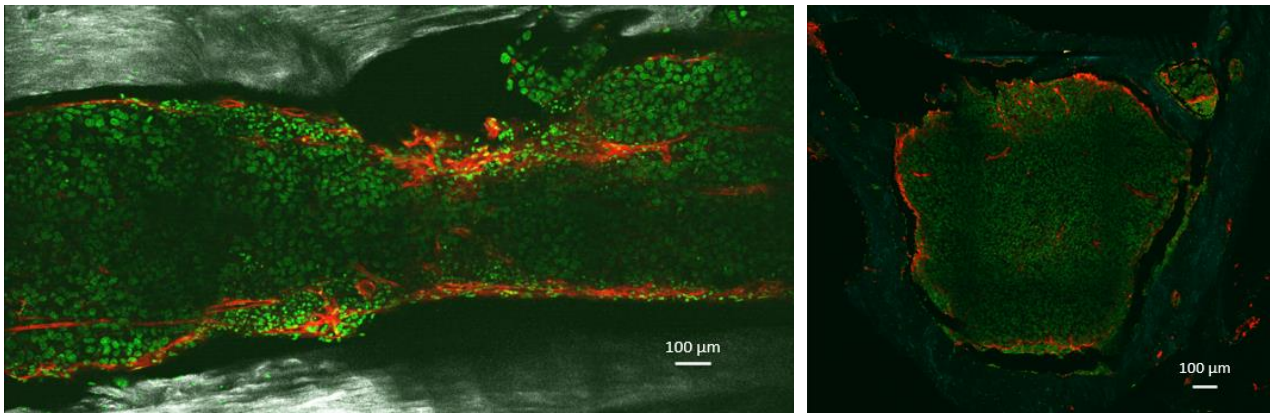


Figure 3: Left: longitudinal section of a tibia with PC3 cells. Right: cross section of a tibia with PC3 cells.

### 3.1.2 Acquisition and Reconstruction of Samples: MPM

MPM offers the possibility to acquire 3D samples through optical sectioning, and to reconstruct their volumes. Specifically, data collected from a bone slice, approximately 300 µm thick, consisted of a series of optical sections, set at 8-10 µm distance, resulting in a sequential stack of images. Besides capturing fluorescence emission, MPM allows capturing nonlinear function of lights. This includes

second harmonic generation (SHG), which is elicited by repetitive biological structures, such as collagen deposited in bone. Overall, the acquisition of bone samples included DAPI and SHG (excitation 920 nm, emission 450/60 nm; grey, Figure 6), tumor cell nuclei (excitation 920, emission 525/50 nm) and blood vessels (excitation 1280 nm, emission 710/80 nm; red). Tumor cell nuclei were easily distinguishable from bone marrow cell nuclei based on their size (~8 times bigger), as reported above. Leveraging Image J software, distinct channels were merged, thereby creating a single stack of images containing both channels (see Figure 4). Additionally, through Image J, a maximum projection was created, resulting from the superimposition of all obtained slices in one single plan (see Figure 4 d). The presence of a dark grid in the images is due to stitching operations performed using Fiji, as MPM acquisition occurs via quadrants, to generate mosaics.

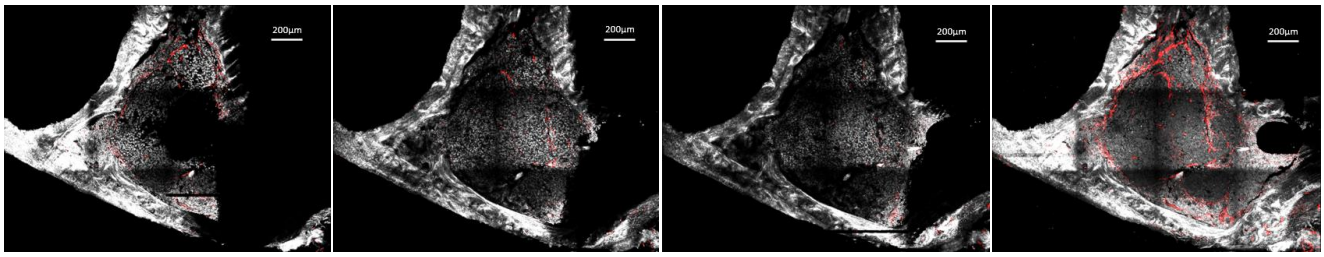


(a) (b) (c) (d)

Figure 4: Data from MPM acquisition, channels merged, cross section of tibiae: (a) slice 8/22; (b) slice 12/22; (c) slice 14/22; (d) z-projection, i.e. superposition of the 22 slices.

### 3.1.3 Analysis of Blood Vessels within Bone Lesions.

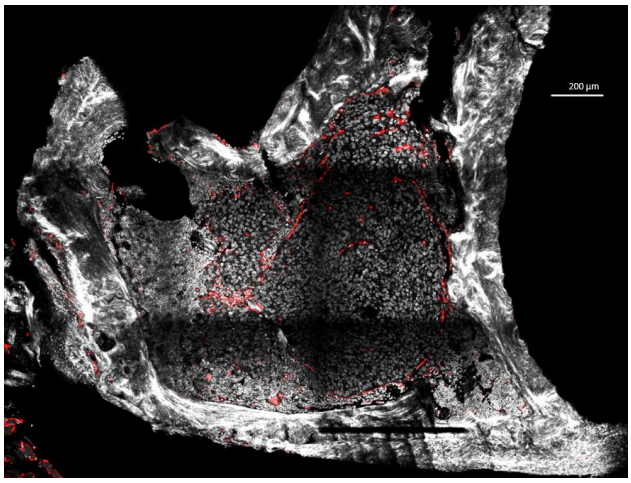


(a) Tibia cross-section, slice 7/16, control.

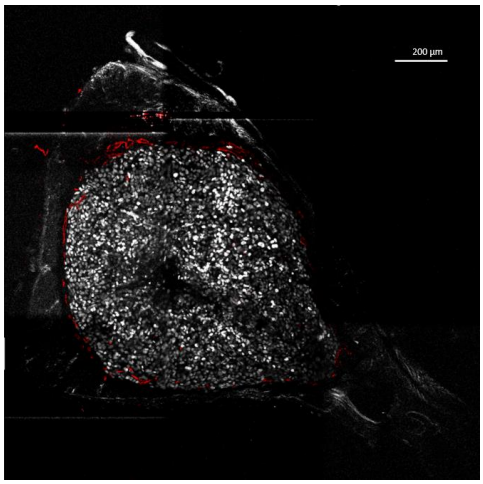


(b) Tibia cross-section, slice 9/19, treatment.

Figure 5: Bone lesion from prostatic tumor, PC3 cell line. Red: BVs, white: PC3 cells, bone marrow cells and bone matrix.

Images of the human prostate cancer cell line acquired by MPM were then analyzed (Figure 5). Initially, we quantified the percentage of area occupied by blood vessels within the tumor area (parameter (a)). This analysis was conducted semi-automatically using ImageJ: the region of interest (ROI) occupied by the tumor was manually defined, the blood vessel channel was duplicated, an 8-bit mask generated, and a Gaussian filter applied to reduce noise, the signal thresholded, and quantified within the ROI using ImageJ. The values obtained are shown in Figure 6. Comparing the results between the control group and the treatment group yielded statistically significant data. Notably, the treated group exhibited a lower percentage of blood vessels within the tumor area compared to the control group, in particular it decreased by 3%. This observation aligns with the mechanism of action of cabozantinib, which involves blocking angiogenesis, thereby impeding tumor progression and resistance.

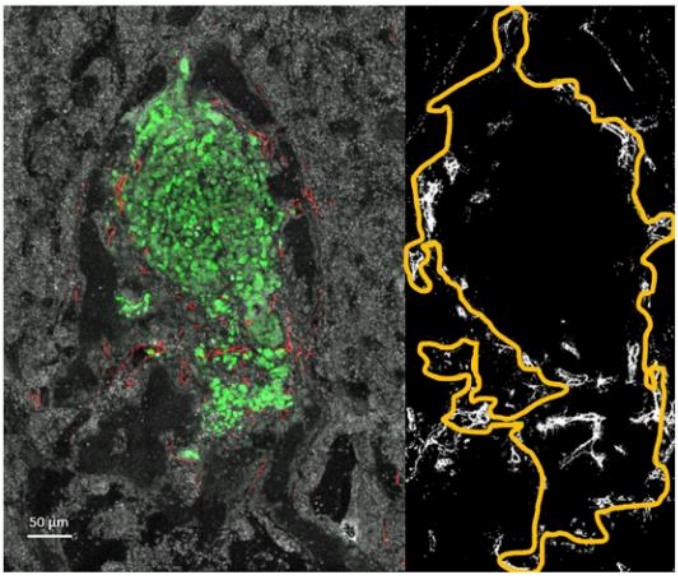


**Percentage of blood vessels within tumor area in the prostate model**

| Control | Treatment |
|---|---|
| 5,09 % | 2,31 % |
| 5,30 % | 2.13 % |
| 5,71 % | 3.23 % |
| 5,91 % | 3.49 % |
| 5,58 % | 3.80 % |

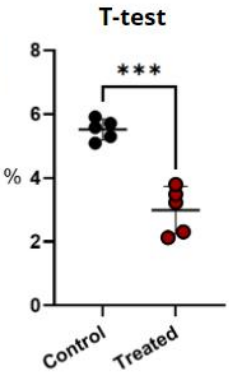


Figure 6: Results from percentage of BVs area within tumor area analysis. From left to right: control tibiae cross-section z-projection (green PC3 cells, red BVs, gray bone marrow cells and bone matrix) and the 8-bit mask with the ROI defined; values obtained in %; T-test graph.

Following this, more blood vessel-related parameters in cabozantinib vs. control treated samples were compared, including their dimensions, i.e. length and width (parameter (b)). This analysis was conducted semi-automatically: the lengths and widths of the blood vessels were manually traced and then calculated using ImageJ. 50 blood vessels/image were quantified. However, in cabozantinib-treated samples were often less than 50/image; so, in these specific instances, all the blood vessels present were analyzed. Although we attempted to automate this process by using an ImageJ plugin called Skeleton, which discriminates image segments (blood vessels) and automatically calculates their length, mutual distance, and other parameters. However, due to the intricate nature of the blood vessel network and the complexity of the images from MPM acquisition, the process was unsuccessful. The semi-automatic analysis of blood vessel dimensions yielded significant results, as shown in Figure 7. Notably, both length and width decreased in the treated group. This suggests that cabozantinib not only affected the number of tumor blood vessels but also their dimensions. Particularly, as highlighted by the frequency distribution of the values quantified,

cabozantinb treatment appeared to impact the vessels with bigger size: the maximum length value dropped from 1000 μm to approximately 600 μm and the maximum width from 400 μm to 50μm, corresponding to a decrease of 40% and 88%. Then, the distance between adjacent blood vessels was compared (parameter (d)), showing non-significant results, see Figure 8.

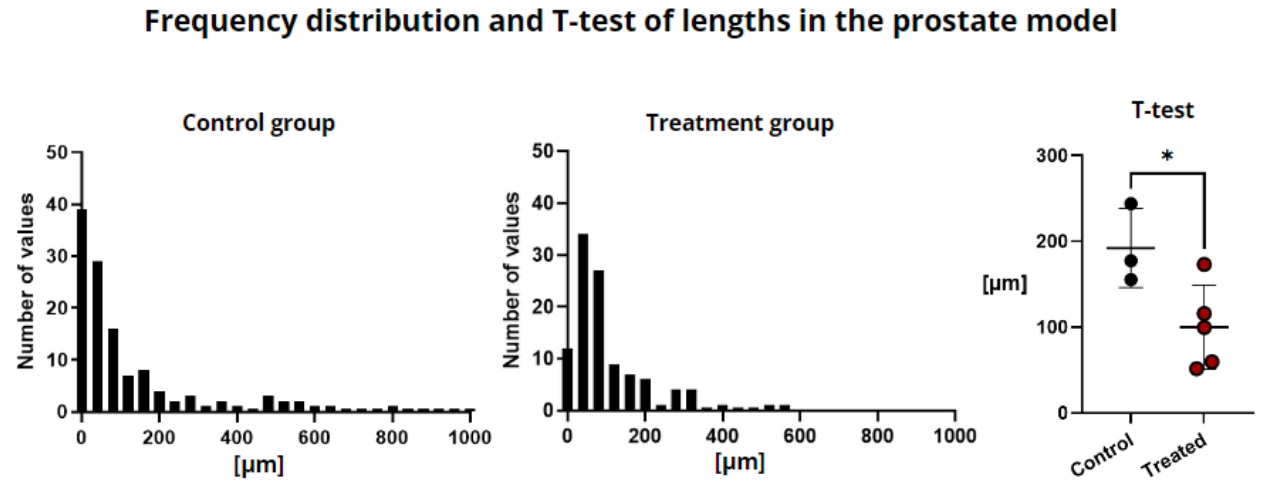


(a)

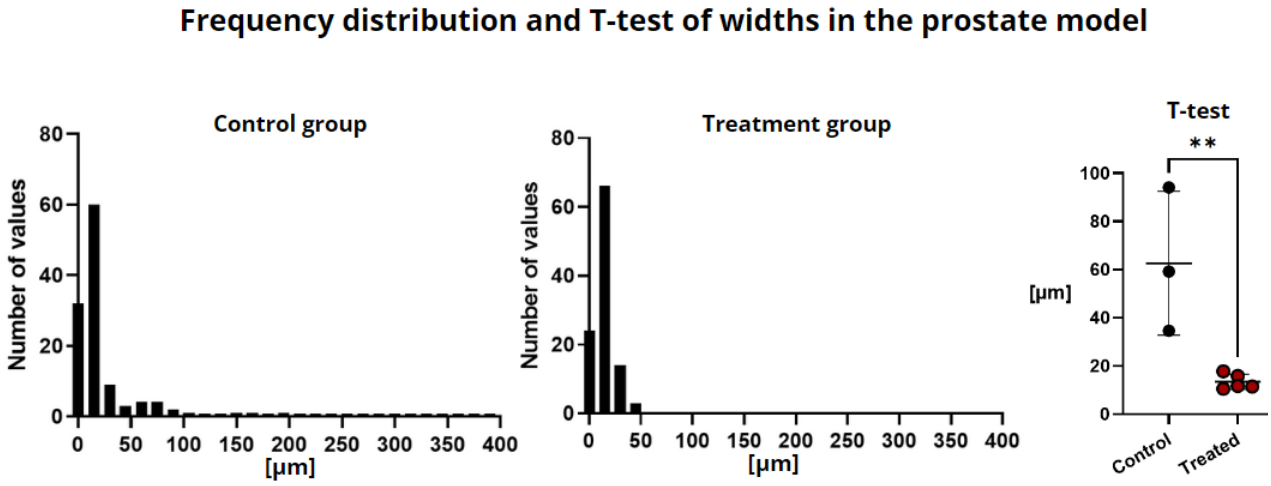


(b)

Figure 7: Results from dimensioning blood vessels size. (a) length; (b) width

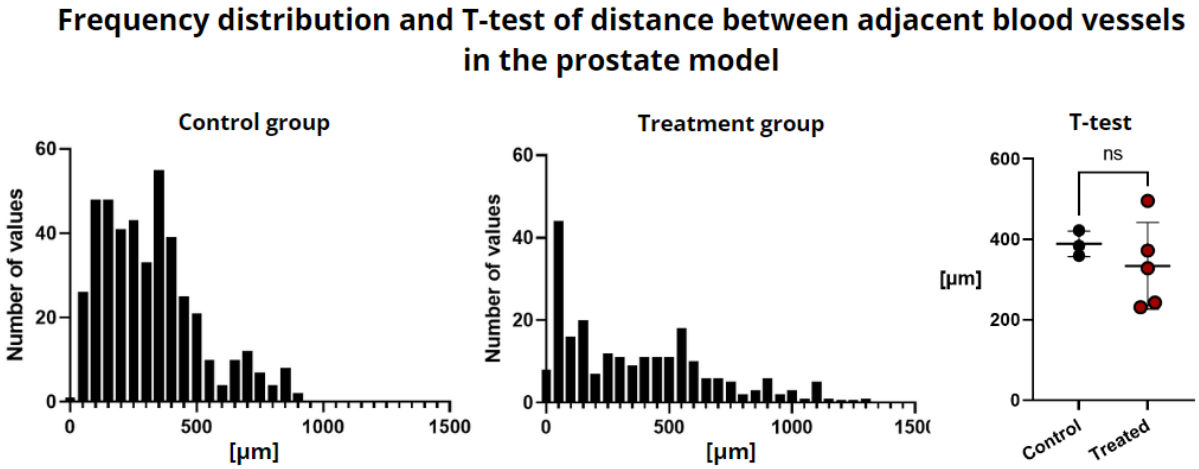


Figure 8. Results from distance between adjacent blood vessels analysis.

Another parameter analyzed was represented by the distance between mitotic cells and the nearest blood vessel (parameter (c)). This parameter did not change with cabozantinib treatment, as shown in Figure 9. This might be due to the fact that mitotic cells require nutrients, and the distance remains independent of the number of blood vessels present. However, what did change was the number of cells in mitosis, as shown in Figure 9: there were fewer in the treated group. This reduction (47%) can be attributed to the action of cabozantinib, which affected the number of vessels, resulting in decreased blood supply for tumor cells and so less mitosis. During this analysis, apoptosis was also observed. Interestingly, while mitosis was frequent, apoptosis phenomena were less common in both the treated and control groups. This observation reflected the dynamics of tumor development: the fewer cells that undergo apoptosis, the more the tumor could grow.

**Number and T-test of mitotic tumor cells in the prostate model**

| Control | Treated |
|---|---|
| 73 | 24 |
| 84 | 23 |
| 105 | 30 |
| 95 | 67 |
| 77 | 57 |

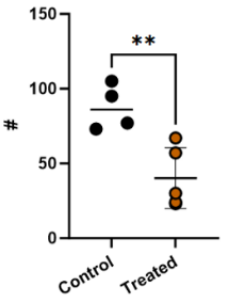


(a)

**Frequency distribution and T-test of distance between mitotic tumor cells and the nearest blood vessel in the prostate model**

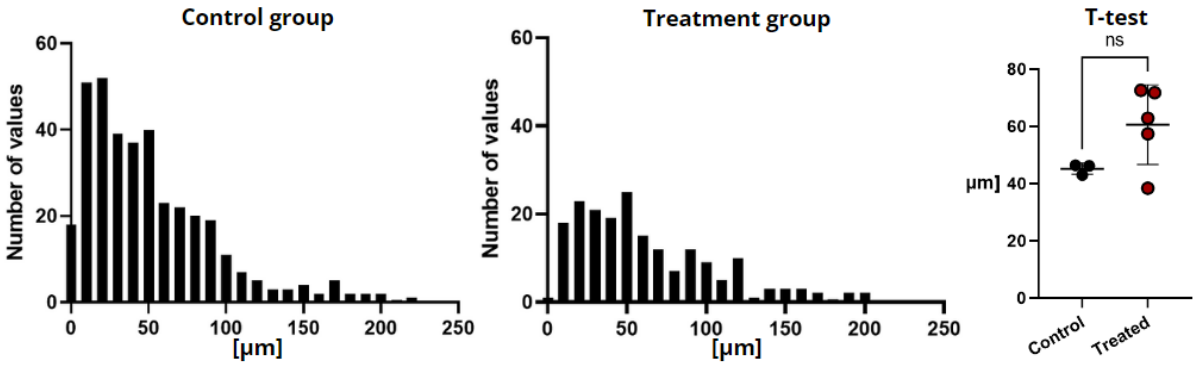


(b)

Figure 9: Result from mitotic tumor cells counting (a) and from distances between mitotic tumor cells and the closest blood vessel analysis (b).

It is important to note that the discrimination of mitotic (and apoptotic) cells was conducted entirely manually, a procedure that is time-consuming and requires expertise. Currently, there is no automated tool for distinguishing mitotic or apoptotic cells. To address this limitation, we started a new research project aimed at developing an artificial intelligence for cell recognition, as detailed in paragraph 3.2.2.

To validate these findings in another tumor type, the renal model was examined. Images showing bone lesions from renal tumors, before and after cabozantinib oral treatment, see Figure 10, were previously acquired by the laboratory team, utilizing the RENCA cell line. The analysis followed the same protocol used for the prostate model, and the results obtained are comparable.

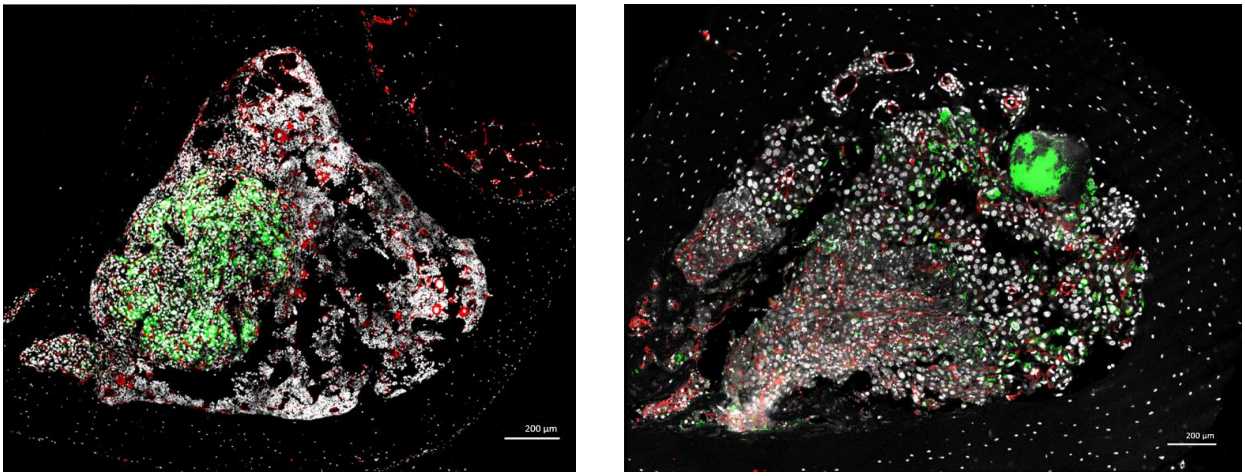


(a) Tibia cross-section, slice 3/7, control. (b) Tibia cross-section, slice 2/4, treatment.

Figure 10: RENCA samples. Red: BVs. Green: RENCA cells. White: bone marrow cells.

The percentage of blood vessels present in the tumor area (parameter (a)), was significantly decreased after cabozantinib treatment (9%), as shown in Figure 11. The statistical significance of these findings is of a lesser magnitude compared to the results from the prostate model. This difference might be due to the PC3 cells employed in the prostate model. Indeed, they exhibited unique behavior in vivo forming tumor clusters with minimal internal blood vessel presence. In these type of bone lesions the blood vessels were predominantly located outside the tumor mass rather than within, reflecting an inherent characteristic of the cell line used. Consequently, the percentage of blood vessels within the tumor area parameter may have been affected by this phenomenon. The percentages obtained from the two control groups differ significantly: the maximum percentage in bone lesions from prostate tumors was 5.91%, whereas in bone lesions from renal tumors it reached 20.48%.

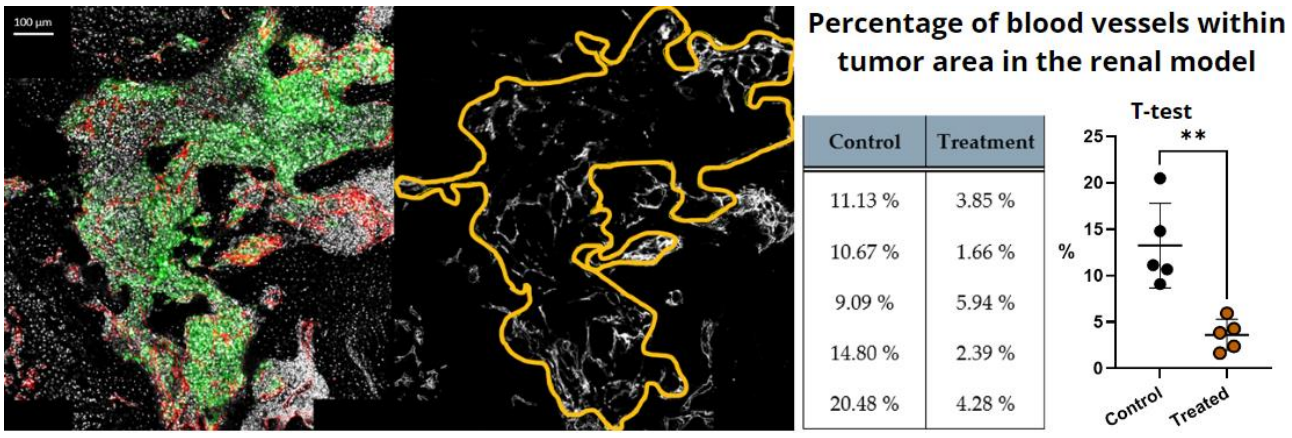


Figure 11: Results from percentage of BVs area within tumor area analysis. From left to right: control tibiae cross-section z-projection (green RENCA cells, red BVs, gray bone marrow cells) and the 8-bit with the ROI defined; values obtained in %; T-test graph.

Following this, the blood vessels-related parameters in cabozantinib vs. control treated samples were compared, such as the size (parameter (b)) and the distance between adjacent blood vessels (parameter (d)) and the results are shown in Figure 12. Cabozantinib has a notable impact on the blood vessel's dimension, and, also from these findings, it appeared to impact the vessels with bigger size: the maximum length value decreased from 800 μm to approximately 200 μm (75% less) and the maximum width from 100 μm to 20 μm (66% less). It is noteworthy to observe the differences in blood vessels network between the two metastatic environments. In the prostatic model, vessels were fewer in number (mean of 5.5%) but longer (1000 μm) and wider (600 μm), and, in the renal model, vessels were more numerous (up to 20.5%) but shorter (500 μm) and narrower (200 μm). The distance between adjacent blood vessels was compared, showing non-significant results.

Finally, the distance from a mitotic cell to the proximal blood vessel (parameter (c))was compared and yielded not significant results, as shown in Figure 13. However, there was a decrease in the number of mitotic cells by 53%. This phenomenon was previously discussed; however, it is interesting to note that the maximum distance of a cell in mitosis from a blood vessel in the renal model is half that found in the prostate model: 100 μm for RENCA cells compared to 200 μm for PC3 cells. During this analysis, apoptotic phenomena were observed, although infrequently, in both the control and treated groups.

In conclusion, cabozantinib has a similar impact on bone lesions from prostate cancer as observed in the renal model: it affected the blood vessels, decreasing their number and size. This effect impedes or delays tumor growth by depriving the cells of the necessary blood supply for replication. Indeed, quantifying the images revealed a decrease in the number of cells entering mitosis. However, the distance from a blood vessel remained consistent even after treatment.

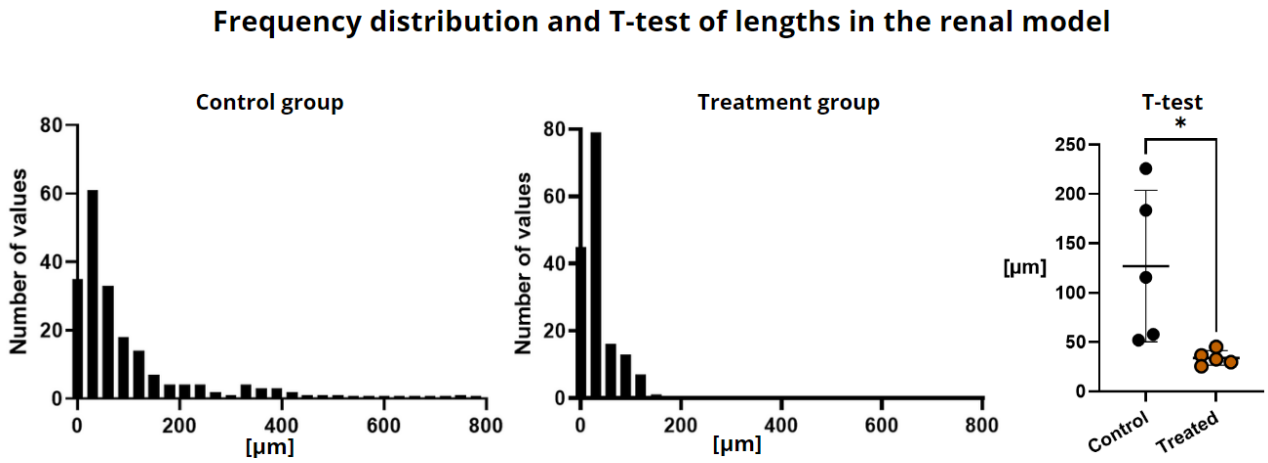


(a)

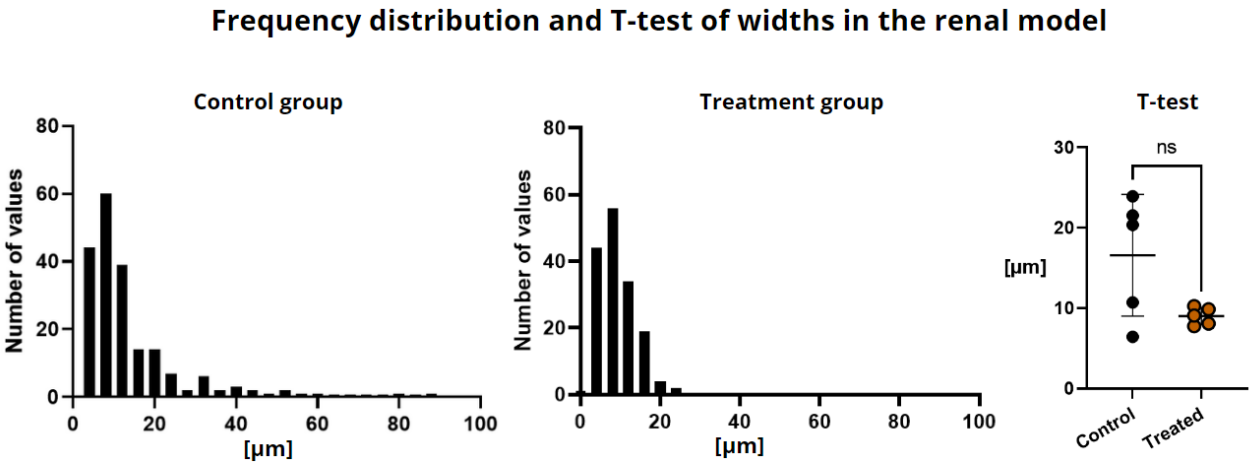


(b)

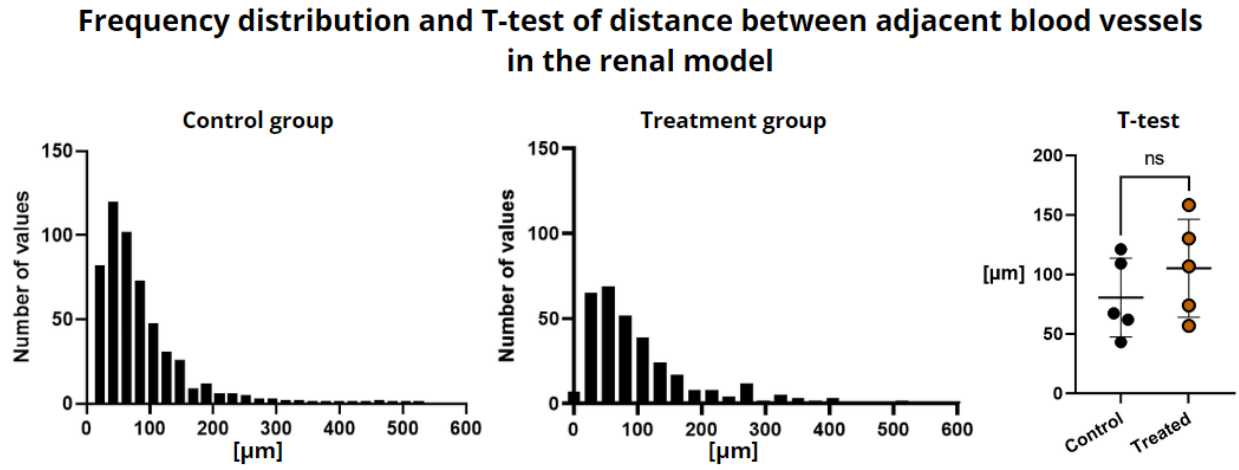


(c)

Figure 12: Results from dimensioning blood vessels network: (a) length; (b) width; (c) mutual distance.

**Number and T-test of mitotic tumor cells in the renal model**

| Control | Treated |
|---|---|
| 22 | 9 |
| 40 | 17 |
| 31 | 13 |
| 27 | 13 |
| 31 | 26 |

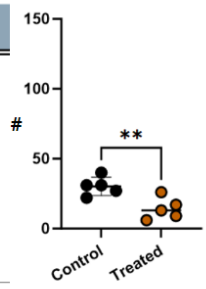


(a)

**Frequency distribution and T-test of distance between mitotic tumor cells and the nearest blood vessel in the renal model**

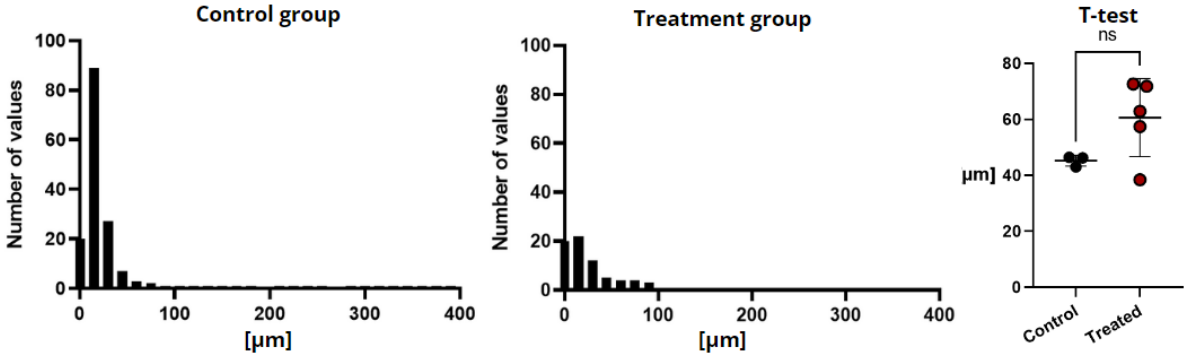


(b)

Figure 13: Results from mitotic tumor cells counting (a) and from distance of MTC from the nearest blood vessel (b).

## 3.2 In Vitro Studies

In the experiments reported above, we explored the correlation between mitotic tumor cells and blood vessels. The discrimination of proliferating (or dying) cells in the images was performed manually, because currently there are no automated tools available to execute this task. As a result, this process was very time-consuming, required significant expertise in identifying mitosis and apoptosis, as well as a very trained eye able to distinguish them within images containing thousands of cells. This prompted us to establish an artificial intelligence-based system for automatic recognition of mitotic and apoptotic nuclei, as part of a larger project in collaboration with the Department of Electronics, Information and Bioengineering. A U-Net neural network was applied. This deep learning algorithm is an unsupervised computational infrastructure that relies on training with ground truth images to be able to achieve automatic identification and segmentation of biological structures of interest. As part of this thesis work, I took care of generating the biological images and segmenting the nuclei used to train the U-Net.

### 3.2.1 Cell Division Characterization

Several experiments were conducted to thoroughly visualize the mechanisms of cell division and apoptosis. For data acquisition, an EVOS system was used, and PC3 dual color cell line was selected as the study model. These cells were chosen because they expressed two fluorochromes: histone H2B-GFP, which allowed nucleus visualization, while DsRed2 allowed cytoplasm visualization. Time lapse recording up to 24 hours were created to visualize the development of mitotic division. Mitosis proceeded as shown in Figure 14: a cell was initially in interphase, preparing to divide and initiate the cell cycle (a). Then, the cell detached, assuming a round shape, and chromatin condensed or aggregated in the nucleus (prophase, (b)). As the cell progressed to metaphase (c), the chromosomes were aligned along the equatorial line of the cell. After this, the chromosomes were ready to separate (anaphase, (d)). The chromatids, each containing identical genetic information, moved in opposite directions, forming the future daughter cells (telophase, (e)). In the final phase, the chromatids were separated and the chromosomes decondensed, resulting in two distinct adhering cells (f). Interestingly, PC3 dual color cell line, progressing from stage (b) to (f), exhibited an average cell division time of 117 minutes, in a range between 60 min and 256 min. Furthermore, the videos also allowed the assessment of mitotic cell percentages at specific time points, revealing a mean value of 4% out of the total.

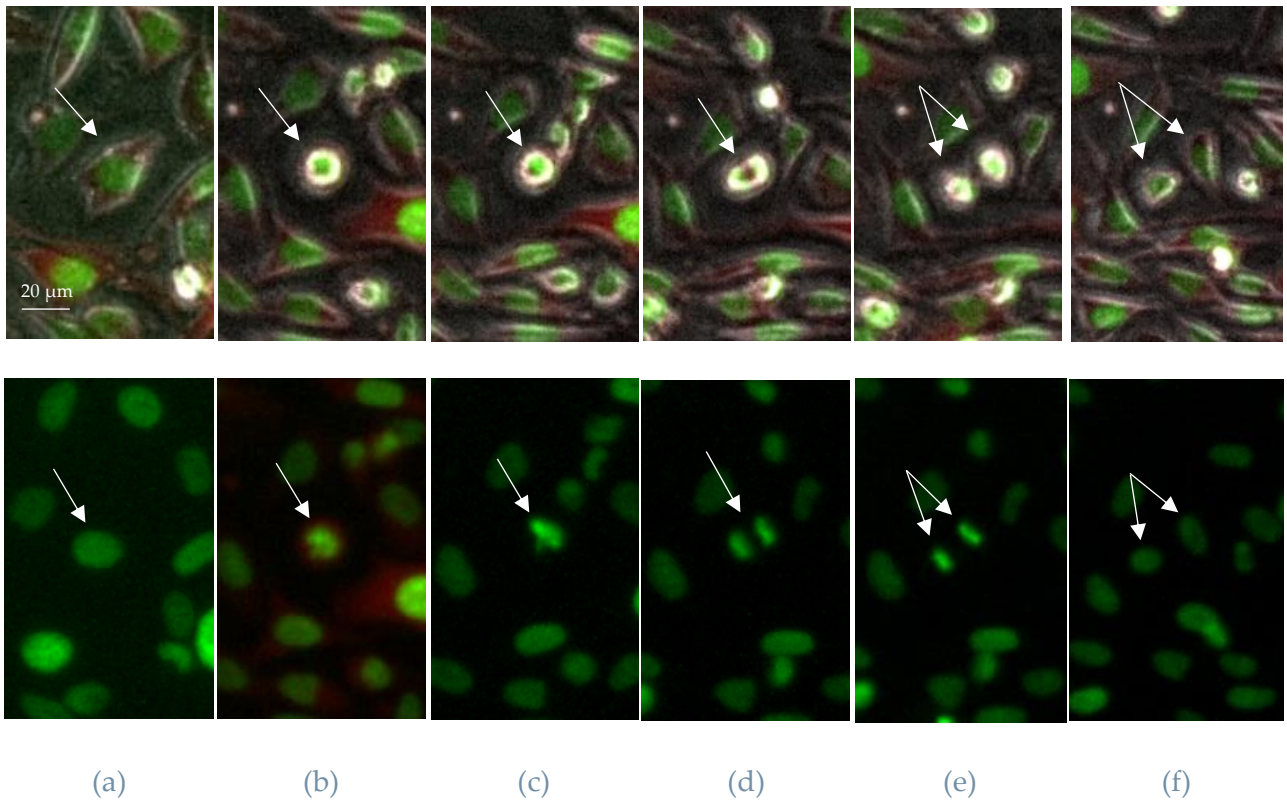


Figure 14: Cell Division Process: (a) interphase, (b) prophase, (c) metaphase, (d) anaphase, (e) telophase, (f) two distinct cells. The cell reported in the figure took 110 minutes to go from (b) to (f). Images were taken from a 24h time lapse performed on an EVOS system, acquiring three channels: one for the nuclei (green, fluorescence), one for the cytoplasm (red, fluorescence) and the third for the phase (grey, bright field). In the first row, the 3 merged channels are shown, in the second row only the nucleus channel is shown.

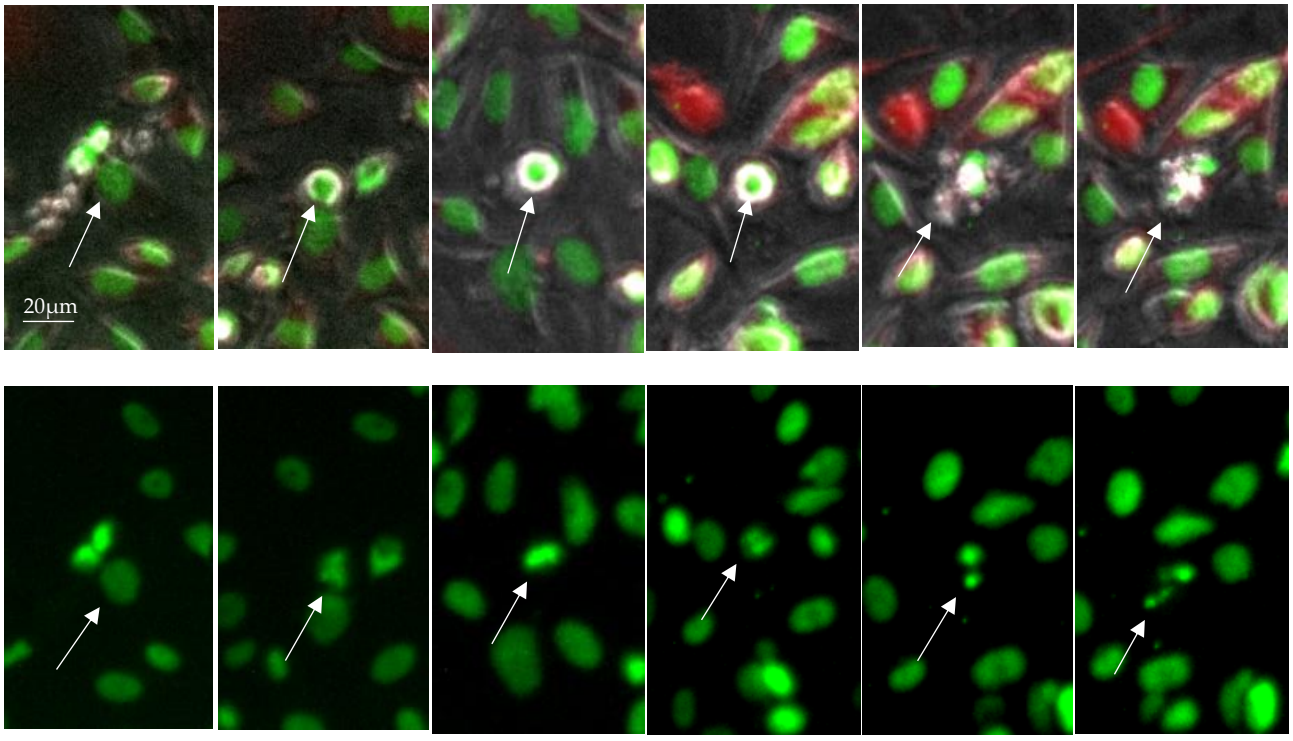


Figure 15: Cellular apoptosis development. (a) interphase; (b) dna aggregated in the nucleo and elongated (c) multiple times before the cell's death (e)(f). From (a) to (f) took 18 hours approximately

Few apoptotic events were observed in vitro, which exhibited a cell death time in the order of hours, up to 18 hours as in the Figure 15. Due to the scarcity of apoptotic cells observed in cell culture, we designed an experiment to induce apoptosis in cells. This experiment, detailed in paragraph 2.3.2, involved the use of three chemotherapy drugs: cisplatin, docetaxel, and doxorubicin. The images collected from the doxorubicin experiment were not quantified because this chemotherapeutic drug induced aberrant nuclei. Therefore, only the resulting images from cisplatin and docetaxel drugs experiment, depicted in Figure 16, were utilized to generate apoptosis discrimination masks for the previously mentioned computational model.

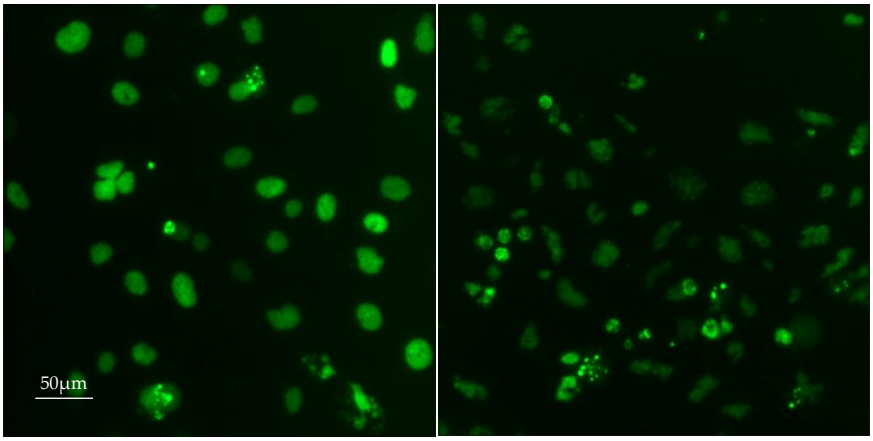


(a) (b)

Figure 16: Images of the chemotherapy drug experiment acquired through EVOS system: cisplatin(a); docetaxel(b).

### 3.2.2 Images Processing for Training U-net System.

To generate masks of mitotic and apoptotic cells to train the U-Net, we captured RGB images using the EVOS system. A total of 80 images were acquired. To perform image segmentation, a frame (patch) was selected measuring 512x512 pixels where mitosis and/or apoptosis events were present (Figure 17 a). The patches were duplicated and saved in their original format, Figure 17 b. From each duplicated patch, an 8-bit mask was generated using ImageJ, then converted into 16-bit image (Figure 17 c), and using Stardist (an ImageJ plugin), all the nuclei were segmented and labelled with different colors (Figure 17 d). Since mitotic and apoptotic cells have irregular shapes, the automatic definition of nuclei through Stardist was often imprecise, requiring manual delineation of nuclei's profiles. Then, the patch was transformed into 8-bit image and nuclei were given a color-code: all the nuclei in interphase were in blue, nuclei undergoing any mitosis phase in yellow and apoptotic nuclei in pink. Subsequently, the segmented patch (at 80% transparency) was superimposed to the original patch. This allowed distinguishing interphase, mitotic and apoptotic nuclei. Any abnormal nucleus was not segmented (Figure 17 I). Both the mask and the original patch served as inputs for the model, (b) and (e) in Figure 17.

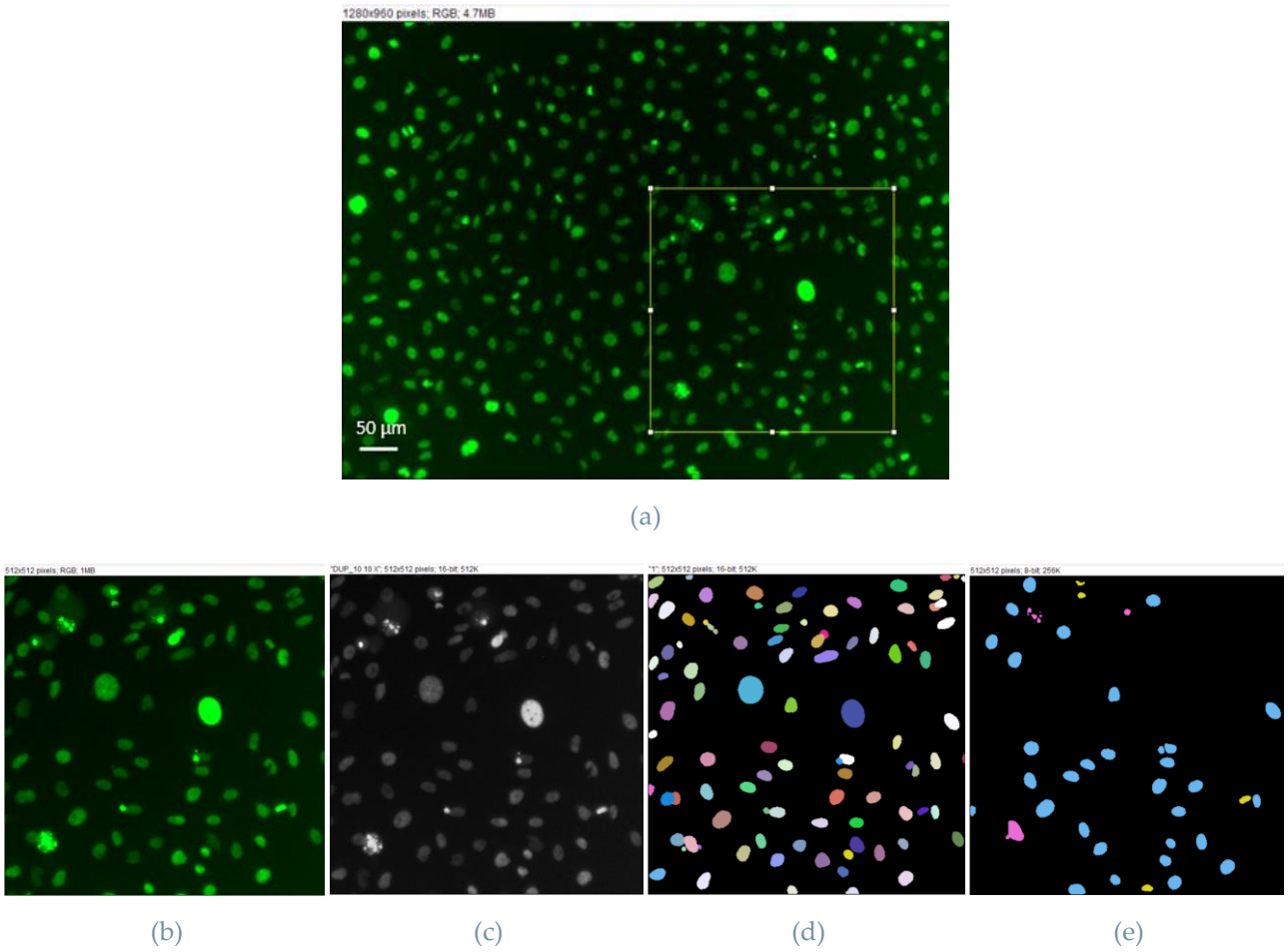


Figure 17: Development of an 8-bit mask starting from RGB images acquired via the EVOS system. Selection of the frame(a); extrapolation of the patch (b); conversion in 16-bit (c); output from Stardist (d); mask(e).

# 4. Discussion

In this study, the impact of cabozantinib within bone lesions resulting from prostate cancer was examined and efficacy was then compared in a renal model. Indeed, despite cabozantinib is being approved for RCC treatment, its effects on bone lesions are obscure, mostly due to the absence of relevant models of bone metastasis. In this study, a newly developed preclinical model for bone metastasis was applied, where nude mice were implanted with human-derived cells, specifically the PC3 cell line, followed by oral administration of cabozantinib. In future studies, a different prostate cancer cell line, such as C42B, could be employed to corroborate these initial results. Regarding the in vivo experiment, my contribution was preparing tumor cells for tibia injection, and administrating cabozantinib orally in the mice, while all the staining experiments and analyses were performed by myself. The samples were processed and cut at a vibratome; they were initially sliced parallel to the longitudinal axis of the bone to achieve a larger field of view. However, when samples were cut parallel to this axis, visualizing the tumor blood vessels was challenging due to the high number of intertwined blood vessels surrounding the tumor mass. Consequently, transverse slicing

was performed to enhance the visualization of blood vessels within the tumor mass. Samples were stained using the immunofluorescence technique and then, images were acquired through MPM. The analysis was performed using ImageJ, resulting in significant findings. The analytic protocol involved the quantification of parameters such as the percentage of blood vessels within the tumor area, their dimensions (length and width), the distance between adjacent blood vessels and the distance between a mitotic tumor cell and the nearest blood vessel. Regarding the second parameter analyzed, i.e. the lengths and widths of blood vessels, 50 blood vessels/image were quantified in the images acquired. However, in cabozantinib-treated samples were often less than 50/image; so, in these specific instances, all the blood vessels present were analyzed. Each parameter was calculated semi-analytically: the region of interest (tumor area) was manually draw, as well as the lengths and widths of the vessels, and the distance between adjacent blood vessels; mitotic and apoptotic tumor cells were identified based on the experience achieved from the in vitro experiments, resulting in a time-consuming process. ImageJ was used to quantify these parameters. The same analysis was conducted also on the images of bone lesions from renal tumor in order to compare the different bone metastasis environment and quantify the changes due to cabozantinib on blood vessels, resulting in new significant findings.

Cabozantinib is a tyrosine kinase inhibitor that primarily targets VEGF receptors, so it exerted its action on blood vessels rather than directly on the tumor cells involved. This mechanism was demonstrated in both tumor models, where it significantly reduced the number and size of blood vessels within the tumor area. It is important to underline that the vascular structure varies across different tumor types, and in our observations, the prostatic model exhibited a less dense vascular network compared to the renal model (5.5% vs. 13% to the tumor area, respectively). Blood vessels also showed different features, with longer and wider vessels (up to 1000 μm and 400 μm, respectively) compared to the renal tumors, which displayed shorter and narrower vessels (up to 800 μm and 90 μm, respectively), consistent with a highly angiogenic tumor type. Considering these distinctions, cabozantinib exhibited a greater impact on the renal model regarding the reduction in vessel number by 9% and vessel length by 75% (as opposed to 3% and 40% in the prostatic model, respectively). Conversely, it showed a more pronounced effect on vessel width reduction in the prostate model, achieving an 88% decrease compared to 66% in the renal model. Interestingly, cabozantinib did not affected the distance of mitotic tumor cells from the nearest blood vessels. Nevertheless, by diminishing the tumor's blood supply, it indirectly decreased the number of mitotic tumor cells, consequently, impairing tumor growth. Specifically, cabozantinib exhibited a similar efficacy in both models, resulting in a 47% decrease of mitotic cells in the prostate model and a 53% decrease of mitotic cells in the renal model. Interestingly, apoptotic cells were not frequent, providing further evidence that cabozantinib exerted no direct influence on tumor cells.

This analysis highlighted that recognizing mitotic (and apoptotic) cells required significant expertise and because there are no automatic tools that discriminate cells in biological images, the entire process was very time-consuming. For this reason, we started to work on a U-Net neural network system, as part of collaboration with the Department of Electronics, Information and Bioengineering. The aim of this work is to apply an artificial intelligence-based system for the automatic recognition and quantification of mitotic and apoptotic nuclei. Specifically, this deep learning algorithm is an unsupervised computational infrastructure that relies on training with ground truth images to be able to achieve automatic identification and segmentation of biological structures of interest. A significant number of mitoses were segmented due to their frequent occurrence in cell cultures. Apoptosis, on the other hand, were a rare event, so an experiment to pharmacologically induce cell

death was conducted, aiming to obtain a comparable number of apoptotic events for images segmentation. This experiment involved the administration of three chemotherapy drugs: Cisplatin, Docetaxel, Doxorubicin. However, segmentation from images treated with Doxorubicin was unusable due to the presence of aberrant nuclei. Images from the remaining two treatments were utilized for apoptosis segmentation and subsequently for training the U-net neural network. Thanks to the experience acquired in identifying apoptotic and mitotic cells, I manually segmented 80 images. Segmenting apoptosis was a more complicated process compared to the segmentation of mitoses. While mitotic events generally exhibit a homogeneous shape and can often be automatically segmented using ImageJ, particularly with the Stardist plugin, apoptotic events present fragmented structures which prevent recognition by automated tools. Consequently, the segmentation of apoptosis was performed manually, resulting in a very time-consuming procedure. However, the entire process serves the overall purpose of automating future analyses.

## 5. Conclusions

The purpose of this study was to study and quantify the impact of cabozantinib in bone lesions originating from prostate and renal cancer. Specifically, the renal model was used as a comparison for evaluating the outcomes obtained from the prostate model analysis, given that cabozantinib is currently approved for treating metastatic renal cell carcinoma. Cabozantinib exhibited similar and comparable effects in both models. Notably, it affected the tumor vascular network, leading to a reduction in the number and size of blood vessels within the tumor area. Additionally, as a secondary effect of the treatment, cabozantinib reduced the number of tumor cells undergoing mitosis, since the blood supply to the area decreased, consequently impeding tumor growth. These findings are noteworthy as cabozantinib demonstrated analogous effects in bone lesions from two different tumors, indicating its efficacy independent from the tumor cell type involved (whether renal or prostatic). To further corroborate our results, future experiments will focus on using different prostate cancer cell lines.

Additionally, to automate the recognition of mitotic (and apoptotic) cells in biological images, we initiated a new project aimed at developing an artificial intelligence-based system capable of discriminating mitotic and apoptotic events. 80 images were quantified for training the network; however, the open challenge remains to quantify additional images to further enhance the network's performance.

## Acknowledgements

I would like to express my deepest gratitude to Dr. Dondossola for her support, for the knowledge transmitted and for practical suggestions during my research and in drafting the essay.

I'm extremely grateful to my advisor prof. Cerveri for his availability and promptness to all my requests.

I am also thankful to my family for their infinite love and constant support that allowed me to complete my university studies.

Finally, I would like to dedicate this achievement to myself, wishing it as the beginning of a long and brilliant professional career.

## References [7]

[1] A. Hyväkkä, O.-S. Kääriäinen and T. Utriainen, "Radium-223 dichloride treatment in metastatic castration-resistant prostate cancer in Finland: A real-world evidence multicenter study," *Cancer Medicine,* vol. 12, pp. 4064-4076, 2023.

[2] S. Turajlic, C. Swanton and C. Boshoff, "Kidney cancer: The next decade," *Journal of Experimental Medicine,* vol. 215, no. 10, pp. 2477-2479, 2018.

[3] S. A. Padalaa, A. Barsoukb, K. C. ThandraKalyan, K. Saginalad, A. Mohammed, A. Vakiti, P. Rawlaf and A. Barsoukg, "Epidemiology of Renal Cell Carcinoma," *World J Oncol,* vol. 11, no. 3, pp. 79-87, 2020.

[4] F. Macedo, K. Ladeira, F. Pinho, N. Saraiva, N. Bonito, L. Pinto and F. Gonçalves, "Bone metastases: an overview.," *Oncol. Rev.,* vol. 11, no. 321, pp. 43-479, may 2017.

[5] R. E. Gray and G. Harris, "Renal Cell Carcinoma: Diagnosis and Management," *American Family Physician,* vol. 99, no. 3, pp. 179-184, 2019.

[6] J. Ban, V. Fock, D. Aryee and H. Kovar, "Mechanisms, Diagnosis and Treatment of Bone Metastases," *Cells,* vol. 10, no. 2944, 2021.

[7] M. Sekhoacha, K. Riet, P. Motloung, L. Gumenku, A. Adegoke and S. Mashele, "Prostate Cancer Review: Genetics, Diagnosis, Treatment Options, and Alternative Approaches.," *Molecules,* vol. 27, no. 17, p. 5730, 5 sept 2022.

[8] P. Berto, A. Aiello, G. Procopio, R. Iacovelli, F. Saverio and F. S. Mennini, "Cabozantinib for first-line treatment of advanced renal cell carcinoma (aRCC) in Italy: a cost-effectiveness analysis," *GIHTAD,* vol. 13, no. 7, 2020.

[9] P. Maroto, C. Porta, J. Capdevila, A. B. Apolo, S. Viteri, C. Rodriguez-Antona, L. Martin and D. Castellano, "Cabozantinib for the treatment of solid tumors: a systematic review," *Therapeutic Advances Med. Oncol.,* vol. 14, p. 175883592211071, gen. 2022.

[10] H. Nguyen, N. Ruppender, X. Zhang, L. Brown, T. Gross, C. Morrissey and e. al, "Cabozantinib Inhibits Growth of Androgen-Sensitive and Castration-Resistant Prostate Cancer and Affects Bone Remodeling," *PLoS ONE,* vol. 9, no. 8, 2013.

[11] A. Patnaik, K. D. Swanson, E. Csizmadia, A. Solanki, N. Landon-Brace, M. P. Gehring, K. Helenius, B. M. Olson, A. R. Pyzer, L. C. Wang, O. Elemento, J. Novak, T. B. Thornley, J. M. Asara, L. Montaser, J. J. Timmons, T. M. Morgan and Y. Wang, "Cabozantinib Eradicates Advanced Murine Prostate Cancer by Activating Antitumor Innate Immunity.," *Cancer Discovery,* vol. 7, no. 7, pp. 750-765, 2017.

[12] M. Santoni, R. Iacovelli, V. Colonna, S. Klinz, G. Mauri and M. Nuti, "Antitumor effects of the multi-target tyrosine kinase inhibitor cabozantinib: a comprehensive review of the preclinical evidence," *EXPERT REVIEW OF ANTICANCER THERAPY,* vol. 21, no. 9, pp. 1029-1054, 2021.

[13] S. Tai, Y. Sun, J. Squires, H. Zhang, W. Oh, C. Liang and J. Huang, "PC3 is a cell line characteristic of prostatic small cell carcinoma," *The Prostate,* vol. 71, no. 15, pp. 1668-1679, 2011.

[14] T. F. Scientific, "EVOS Cell imaging System | Thermo Fisher Scientific - US," Thermo Fisher Scientific Inc., 2023. [Online]. Available: https://www.thermofisher.com/it/en/home/life-science/cell-analysis/cellular-imaging/evos-cell-imaging-systems.html. [Accessed 12 Dicembre 2023].

[15] S. Dasari and P. B. Tchounwou, "Cisplatin in cancer therapy: molecular mechanisms of action," *Eur. J. Pharmacol.,* vol. 740, pp. 364-378, ott. 2014.

[16] K. A. Lyseng-Williamson and C. Fenton, "Docetaxel," *Drugs,* vol. 65, pp. 2513-2531, 2005.

[17] D. W. Piston, T. J. Fellers and M. W. Davidson, "MicroscopyU," 2023 Nikon Instruments Inc., [Online]. Available: https://www.microscopyu.com/techniques/multi-photon/multiphoton-microscopy. [Accessed 31 12 2023].

[18] C. Schneider, W. Rasband and K. Eliceiri, "NIH Image to ImageJ: 25 years of image analysis.," *Nat Methods,* p. 671–675, 2012.

[19] M. Dubey, "Nude Mice - More than What Meets the Naked Eye," 23 December 2019. [Online]. Available: https://www.jax.org/news-and-insights/jax-blog/2019/December/nude-mice. [Accessed 21 December 2023].

[20] M. Megías, P. Molist and M. Pombal, "Atlas of Plant and Animal Histology.," University of Vigo - Faculty of Biology, 1 08 2022. [Online]. Available: http://mmegias.webs.uvigo.es/index.html. [Accessed 29 12 2023].

[21] K. Im, S. Mareninov, M. F. P. Diaz and W. H. Yong, "An introduction to Performing Immunofluorescence Staining," in *Methods in Molecular Biology*, vol. 1897, Spriger New jork, 2019, pp. 299-311.

[22] M. Bersanelli, S. Buti, A. Ghidini, M. Tiseo and F. Petrelli, "A metanalysis on cabozantinib and bone metastases: true story or commercial gimmick?," *Anti-Cancer Drugs,* vol. 31, no. 3, pp. 211-215, march 2020.

[23] O. Tacar, P. Sriamornsak and C. R. Dass, "Doxorubicin: an update on anticancer molecular action, toxicity and novel drug delivery systems," *J. Pharmacy Pharmacol,* vol. 65, no. 2, p. 157–170, ago. 2012.

[24] D. Castellano, A. B. Apolo, C. Porta, J. Capdevila, S. Viteri, C. Rodriguez-Antona, L. Martin and P. Maroto, "Cabozantinib combination therapy for the treatment of solid tumors: a systematic review," *Medical Oncology,* vol. 14, pp. 1-37, 2022.

[25] E. Dondossola and P. Friedl, "Host responses to implants revealed by intravital microscopy," *Nature Reviews Materials* , pp. 6-22, 2022.